Illustration of transition path theory on a collection of simple examples

Philipp Metzner[a)] and Christof Schütte[b)]
Department of Mathematics and Computer Science, Free University Berlin, Arnimallee 2-6,
D-14195 Berlin, Germany

Eric Vanden-Eijnden[c)]
Courant Institute of Mathematical Sciences, New York University, New York, New York 10012

Transition path theory (TPT) has been recently introduced as a theoretical framework to describe the reaction pathways of rare events between long lived states in complex systems. TPT gives detailed statistical information about the reactive trajectories involved in these rare events, which are beyond the realm of transition state theory or transition path sampling. In this paper the TPT approach is outlined, its distinction from other approaches is discussed, and, most importantly, the main insights and objects provided by TPT are illustrated in detail via a series of low dimensional test problems. © *2006 American Institute of Physics*. [DOI: 10.1063/1.2335447]

I. INTRODUCTION

Rare but important transition events between long lived states are a key feature of many systems arising in physics, chemistry, biology, etc. Since the 1930s transition state theory (TST) and evolutions thereof based on the reactive flux formalism have provided the main theoretical framework for the description of these events[1–5] (see also Refs. 6 and 7). In principle, TST allows one to compute the transition rate of a reaction: the TST rate gives a first estimate of the reaction rate which can then be corrected via the reactive flux formalism to obtain the actual frequency of the reaction. Performing this computation in practice, however, may prove very challenging, and this difficulty is related to a deficiency of the theory. TST is based on partitioning the system into two, leaving the reactant state on one side of a dividing surface and the product state on the other, and the theory only tells how this surface is crossed during the reaction. As a result, TST provides very little information about the mechanism of the transition, which has bad consequences, e.g., if this mechanism is totally unknown *a priori*. In this case, it is difficult to choose a suitable dividing surface and a bad choice will lead to a very poor estimate of the rate by TST (too many spurious crossings of the surface that do not correspond to actual reactive events). The TST estimate is then extremely difficult to correct. The situation is even worse when the reaction is of diffusive type, since in this case all surfaces are crossed many times during a single reactive event and there is simply no good TST dividing surface that exists.

How to go beyond TST and describe rare events whose mechanism is unknown *a priori* is an active area of research and several new techniques have been developed to tackle these situations. Most notable among these techniques are the transition path sampling (TPS) technique of Geissler and

co-workers[8,9] and the action method of Elber *et al.*[10,11] which allow to sample directly the ensemble of reactive trajectories, i.e., the trajectories by which the reaction occurs. The mechanism of the reaction and possibly its rate can then be obtained *a posteriori* by analyzing the ensemble of reactive trajectories. It is worth pointing out, however, that these operations are far from trivial. TPS or the action method *per se* does not tell how this analysis must be done and simple inspection of the reactive trajectories may not be sufficient to understand the mechanism of the reaction. This may sound paradoxical at first, but the problem is that the reactive trajectories may be very complicated objects from which it is difficult to extract the quantities of real interest such as the probability density that a reactive trajectory be at a given location in state space, the probability current of these reactive trajectories, or their rate of appearance. In a way, this difficulty is the same that one would encounter having generated a long trajectory from the law of classical mechanics but ignoring all about statistical mechanics: how to interpret this trajectory would then be unclear. Similarly, the statistical framework to interpret the reactive trajectories is not given by the trajectories themselves, and further analysis beyond TPS or the action method is necessary (for an attempt in this direction, see Ref. 12).

Recently, a theoretical framework to describe the statistical properties of the reactive trajectories has been introduced.[13,14] This framework, termed transition path theory (TPT), goes beyond standard equilibrium statistical mechanics and account for the nontrivial bias that the very definition of the reactive trajectories imply—they must be involved in a reaction. The main objects provided by TPT to describe the reactive trajectories are their probability density function, their probability current and flux, and their rate. TPT is the theoretical background beyond the string method,[15–20] which is a numerical technique to compute the statistical properties of the reactive trajectories directly (that is, without having to identify these trajectories themselves beforehand as in TPS or the action method) in complicated

---

a)Electronic mail: metzner@math.fu-berlin.de
b)Electronic mail: schuette@math.fu-berlin.de
c)Electronic mail: eve2@cims.nyu.edu

125, 1-1

systems with many degrees of freedom. The purpose of the present paper is different: here we aim at illustrating TPT via low dimensional examples. While these examples are obviously simplistic compared to those of actual interests in applications, they already display a wide variety of behaviors that allow to illustrate the power of TPT and the advantage that this formalism offers overlooking directly at the reactive trajectories themselves. In the remainder of this paper, we will first recall the main aspects of TPT in Sec. II, leaving the more technical aspects of the theory to the Appendix; we also explain briefly how the various quantities of TPT were computed on the simple examples. The predictions of TPT on these examples are described in Secs. III–VII. In Sec. III we consider an example in which a particle diffuses by overdamped dynamics in a two-dimensional double-well potential. In Sec. IV, we consider a two-dimensional example where the barrier between the metastable states is purely entropic. In Sec. V, we consider an example proposed by Park *et al.* in Ref. 21 in which a particle diffuse by overdamped dynamics in a two-dimensional triple-well potential (two deep wells and one shallow one): in this example, the preferred pathway of reaction switches from one channel to another depending on the temperature. In Sec. VI, we consider a two-dimensional example in which one variable is slow and the other is fast. Finally, in Sec. VII, we consider an example of a particle moving by Langevin dynamics in a double-well potential and investigate how the mechanism of reaction depends on the friction coefficient. In all examples, we give the probability density of the reactive trajectories, and compute their probability current and flux, and their rate via TPT. We also compare these predictions with the results of direct numerical simulations of the dynamical system. Finally, some concluding remarks are given in Sec. VIII.

II. A SHORT ACCOUNT OF TRANSITION PATH THEORY

In this section, we give a short account of TPT. For more details, we refer the reader to the Appendix or to the original references.[13,14] For simplicity, in Sec. II A we first describe the theory in the case of a system governed by overdamped (or Smoluchowsky) dynamics. Then, in Sec. II B we show how the theory generalizes to the case of a system described by the Langevin equation.

A. TPT in the overdamped case

Consider a system described by the overdamped equation,

$$\gamma_i \dot{x}_i(t) = -\frac{\partial V(x(t))}{\partial x_i} + \sqrt{2k_B T \gamma_i}\, \eta_i(t), \tag{1}$$

where $x=(x_1, x_2, \ldots, x_n) \in \mathbb{R}^n$ denotes the position of the particles, $V(x)$ is the potential, γ_i is the friction coefficient on x_i, T is the temperature, and $\eta_i(t)$ is a white noise, i.e., a Gaussian process with mean zero and covariance $\langle \eta_i(t) \eta_j(s) \rangle = \delta_{ij}\delta(t-s)$. (1) arises in the high friction limit of the Langevin equation given below in (13). (1) is simpler than (13) because if $x(t)$, $-\infty < t < \infty$, is an equilibrium trajectory of (1), then the time reversed trajectory $x(-t)$ is statistically
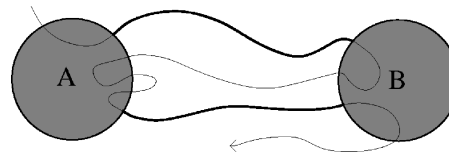

FIG. 1. Schematic representation of the reactant state A, the product state B, and a piece of an equilibrium trajectory (shown in thin black). The subpieces connecting ∂A to ∂B (shown in thick black) are each a reactive trajectory, and the collection of all of them is the ensemble of reactive trajectories.

indistinguishable from $x(t)$, a property that is referred to as the time reversibility of the solution of (1) [in contrast, if $(x(t), v(t))$ is an equilibrium trajectory of (13), the time reversed trajectory which is statistically equivalent to it is $(x(-t), -v(-t))$, i.e., we must revert the velocity as we revert time, and this introduces some complications that are dealt with in Sec. II B].

The solution of (1) is ergodic with respect to the Boltzmann-Gibbs probability density function, which means that, given any suitable observable $\phi(x)$, we have

$$\lim_{T \to \infty} \frac{1}{2T} \int_{-T}^{T} \phi(x(t))dt = Z^{-1} \int_{\mathbb{R}^n} \phi(x)e^{-\beta V(x)}dx, \tag{2}$$

where $\beta = 1/k_B T$ and $Z = \int_{\mathbb{R}^n} e^{-\beta V(x)}dx$. (2) is a property of any generic trajectory in the system which, during the time interval $[-T, T]$, will be involved in any given reaction many times when T is large (and infinitely often as $T \to \infty$). Suppose, however, that one is not interested in the statistical properties of such a generic trajectory but rather in the statistical properties that this trajectory displays while involved in a reaction. This question can be made precise as follows. Suppose that $A \subset \mathbb{R}^n$ and $B \subset \mathbb{R}^n$ are two regions in configuration space that characterize the system while it is in the reactant and the product states, respectively, of a given reaction. Then, given any generic trajectory, $x(t)$, $-\infty < t < \infty$, we can prune this trajectory as illustrated in Fig. 1 to consider only the pieces of this trajectory that connect ∂A (the boundary of A) to ∂B (the boundary of B). Each such piece is a reactive trajectory and the collection of all of them is the ensemble of reactive trajectories. By ergodicity, the statistical properties of this ensemble are independent of the particular trajectory used to generate the ensemble, and these properties are the object of TPT. We summarize them next.

What is the probability density to observe a reactive trajectory at position $x \notin A \cup B$ at time t, conditional on it being reactive at time t? Let $q(x)$ be the so-called committor function, that is, the probability that the trajectory starting from $x \notin A \cup B$ reaches first B rather than A. Given $q(x)$ and exploiting both the Markov property of the dynamics and its time reversibility, it is easy to see that the probability density to observe a reactive trajectory at point $x \notin A \cup B$ at time t is the probability density to observe any trajectory (reactive or not) at point x, which is $Z^{-1}e^{-\beta V(x)}$, times the probability that it will be reactive, which is $q(x)(1-q(x))$ since it must go to B rather than A next [this explains the factor $q(x)$] and it needs to come from A rather than B last [this explains the

factor $1 - q(x)$, accounting for time reversibility]. Summarizing, we have that the probability density to observe a reactive trajectory at point $x \notin A \cup B$ at time t is

$$Z^{-1}e^{-\beta V(x)}q(x)(1 - q(x)). \tag{3}$$

This means that the total probability that the trajectory be reactive at time t is

$$Z_{AB} = Z^{-1}\int_{\Omega_{AB}} e^{-\beta V(x)}q(x)(1 - q(x)), dx, \tag{4}$$

where $\Omega_{AB} = \mathbb{R}^n \backslash (A \cup B)$, and the probability density to observe a reactive trajectory at point $x \notin A \cup B$ at time t conditional on it being reactive at time t is

$$\rho_{AB}(x) = Z_{AB}^{-1}Z^{-1}e^{-\beta V(x)}q(x)(1 - q(x)). \tag{5}$$

This expression was first derived in Ref. 12.

The probability density $\rho_{AB}(x)$ is not the only quantity of interest as it may not be sufficient to characterize the reaction pathway. To get a better understanding of this pathway, we may also ask about the probability current of reactive trajectories. Roughly, this current is such that, integrated over any surface in Ω_{AB}, it gives the probability flux of reactive trajectories across this surface, that is, the net balance between the number of trajectories that crosses this surface in one direction minus the number of them that crosses this surface in the opposite direction during an infinitesimal time interval [the precise definition is given in (A12) in the Appendix]. As shown in the Appendix, this flux is the vector field whose ith component is given by

$$J_{AB,i}(x) = Z^{-1}e^{-\beta V(x)}k_B T\gamma_i^{-1}\frac{\partial q(x)}{\partial x_i}. \tag{6}$$

This vector field is divergence-free, $\Sigma_{i=1}^n \partial J_{AB,i}/\partial x_i = 0$, consistent with the fact that the total probability flux of reactive trajectories across a closed surface in Ω_{AB} is zero (all the trajectories that go in the set enclosed by this surface must come out),

$$0 = \int_{\partial C} \hat{n}_{\partial C}(x)J_{AB}(x)d\sigma_{\partial C}(x), \quad C \subset \Omega_{AB}, \tag{7}$$

where $\hat{n}_{\partial C}(x)$ denotes the unit normal to ∂C pointing outward C and $d\sigma_{\partial C}(x)$ is the surface element on ∂C. On the other hand, the total flux across any dividing surface S in Ω_{AB} (i.e., any surface that leaves A on one side and B on the other) is nonzero and equal to the mean frequency of observing reactive trajectories,

$$k_{AB} = \int_S \hat{n}_S(x)J_{AB}(x)d\sigma_S(x), \tag{8}$$

where $\hat{n}_S(x)$ denotes the unit normal to S pointing toward B and $d\sigma_S(x)$ is the surface element on S. k_{AB} is also the rate of the reaction. As shown in the Appendix, (8) can be reexpressed as a volume integral,

$$k_{AB} = Z^{-1}k_B T\int_{\Omega_{AB}} \sum_{i=1}^n \gamma_i^{-1}\left(\frac{\partial q(x)}{\partial x_i}\right)^2 e^{-\beta V(x)}dx. \tag{9}$$

Another quantity of interest which can be extracted from the probability current of reactive trajectories are the streamlines of this current. These are the solutions of

$$\frac{dx_i(\tau)}{d\tau} = J_{AB,i}(x(\tau)). \tag{10}$$

(The "time" τ in this equation is artificial and unrelated to the physical time t.) Solving (10) with the initial condition $x(0) \in \partial A$ one obtains a streamline connecting A to B; the ensemble of streamlines associated with all initial conditions $x(0) \in \partial A$ forms a bundle of curves in Ω_{AB} whose union is Ω_{AB} itself. The streamlines of the current are an indicator of the average trend of the reactive trajectories, and they allow to define reaction (or transition) tubes connecting A to B carrying a certain percentage of the probability flux of reactive trajectories. Indeed, suppose that $\partial' A \subset \partial A$ is a subset of the boundary of the reactant state A across which $p\%$ of the probability flux of reactive trajectories go, i.e.,

$$\int_{\partial'A} \hat{n}_{\partial A}(x)J_{AB}(x)d\sigma_{\partial A}(x) = \frac{p}{100}\int_{\partial A} \hat{n}_{\partial A}(x)J_{AB}(x)d\sigma_{\partial A}(x)$$

$$\equiv \frac{pk_{AB}}{100}, \tag{11}$$

where we used (8) and the fact that ∂A is a dividing surface between A and B. Then, the ensemble of streamlines obtained by solving (10) for all initial conditions $x(0) \in \partial'A$ forms a reaction tube connecting A and B which carries $p\%$ of the probability flux of reactive trajectories. Sometimes, a rather localized tube can be found which carries a high percentage of the flux: then, the reactive trajectories must remain inside this tube with high probability, i.e., it is the preferred channel for the reaction.

The formula above clearly indicates that the committor function $q(x)$ is the key quantity to describe the statistical properties of the reactive trajectories. For a system whose dynamics is described by (1), it is a well-known result of stochastic processes theory that $q(x)$ satisfies the so-called backward Kolmogorov equation,[22]

$$0 = \sum_{i=1}^n \left(-\gamma_i^{-1}\frac{\partial V(x)}{\partial x_i}\frac{\partial q(x)}{\partial x_i} + k_B T\gamma_i^{-1}\frac{\partial^2 q(x)}{\partial x_i^2}\right),$$

$$q(x)|_{x \in \partial A} = 0, \quad q(x)|_{x \in \partial B} = 1. \tag{12}$$

In large dimensional systems, the main question of interest then becomes how to solve (12), which is a highly nontrivial problem since (12) is a partial differential equation for a function of many variables. The string method is a way to deal with this issue. In the context of the two-dimensional examples considered in this paper, however, standard numerical techniques based on discretizing (12) by finite difference or finite element can be applied, as briefly explained in Sec. II C.

B. TPT in the Langevin case

The results of TPT can be generalized to systems described by the Langevin equation,

$$\dot{x}_i(t) = v_i(t),$$

$$\tag{13}$$

$$m_i\dot{v}_i(t) = -\frac{\partial V(x(t))}{\partial x_i} - \gamma_i v_i(t) + \sqrt{2k_BT\gamma_i}\,\eta_i(t),$$

where $v=(v_1,v_2,\ldots,v_n)\in\mathbb{R}^n$ is the velocity of the particles, m_i is the mass of x_i, and the other quantities are as in (1). As mentioned earlier, the main difference is that reverting time in (13) now amounts to reverting both t and v. Reactive trajectories can be introduced similarly as earlier, except that they must be defined in phase space (x,v) rather than configuration space x since the dynamics of $(x(t),v(t))$ is Markov but the one of $x(t)$ alone is not. Similarly, both the reactant $\mathcal{A}\subset\mathbb{R}^n\times\mathbb{R}^n$ and the product state $\mathcal{B}\subset\mathbb{R}^n\times\mathbb{R}^n$ must be subsets in phase-space (x,v) rather than configuration space x. Both a forward committor function $q(x,v)$ [giving the probability that the trajectory starting at (x,v) reaches first $\mathcal{A}$ rather than $\mathcal{B}$] and a backward committor function $q_b(x,v)$ [giving the probability that the trajectory arriving at (x,v) came last from $\mathcal{A}$ rather than $\mathcal{B}$] must be introduced; by

symmetry, the later can be related to the former simply as

$$q_b(x,v) = 1 - q(x,-v).$$

$$\tag{14}$$

In terms of these quantities, the probability density to observe a reactive trajectory at (x,v) at time t conditional on the trajectory being reactive at time t now becomes [compare (5)]

$$\varrho_{AB}(x,v) = \mathcal{Z}_{AB}^{-1}\mathcal{Z}^{-1}e^{-\beta H(x,v)}q(x,v)q_b(x,v),$$

$$\tag{15}$$

where $H(x,v)=\frac{1}{2}\sum_{i=1}^n m_iv_i^2+V(x)$ is the Hamiltonian, $\mathcal{Z}=\int_{\mathbb{R}^n\times\mathbb{R}^n}e^{-\beta H(x,v)}dxdv$ is the partition function, and $\mathcal{Z}_{AB}$ is the total probability that the trajectory be reactive at time t [compare (4)],

$$\mathcal{Z}_{AB} = \mathcal{Z}^{-1}\int_{\Omega_{AB}} e^{-\beta H(x,v)}q(x,v)q_b(x,v)dxdv,$$

$$\tag{16}$$

where $\Omega_{AB}=\mathbb{R}^n\times\mathbb{R}^n\backslash(\mathcal{A}\cup\mathcal{B})$. The probability current of the reactive trajectories can be obtained as well [see the Appendix and compare (6)],

$$\mathcal{J}_{AB,i}^x(x,v) = \mathcal{Z}^{-1}e^{-\beta H(x,v)}q(x,v)q_b(x,v)v_i,$$

$$\mathcal{J}_{AB,i}^v(x,v) = \mathcal{Z}^{-1}e^{-\beta H(x,v)}\left(-q(x,v)q_b(x,v)m_i^{-1}\frac{\partial V(x)}{\partial x_i} - k_BT\gamma_i m_i^{-1}q(x,v)\frac{\partial q_b(x,v)}{\partial v_i} + k_BT\gamma_i m_i^{-1}q_b(x,v)\frac{\partial q(x,v)}{\partial v_i}\right),$$

$$\tag{17}$$

where $\mathcal{J}_{AB,i}^x(x,v)$ and $\mathcal{J}_{AB,i}^v(x,v)$ are the components of the current in the directions of x_i and v_i, respectively. Out of the current the reaction rate can be computed [compare (8)],

$$k_{AB} = \int_{\mathcal{S}} \hat{n}_S(x,v)\mathcal{J}_{AB}(x,v)d\sigma_S(x,v),$$

$$\tag{18}$$

where $\mathcal{S}$ is a dividing surface in phase space between $\mathcal{A}$ and $\mathcal{B}$, $\hat{n}_S(x,v)$ is the unit normal on $\mathcal{S}$ pointing toward $\mathcal{B}$, and $d\sigma_S(x,v)$ is the surface element on $\mathcal{S}$. (18) can be reexpressed as a volume integral as [compare (9)]

$$k_{AB} = \mathcal{Z}^{-1}k_BT\int_{\Omega_{AB}} \sum_{i=1}^n \gamma_i m_i^{-1}\left(\frac{\partial q(x,v)}{\partial v_i}\right)^2 \times e^{-\beta H(x,v)}dxdv.$$

$$\tag{19}$$

The streamlines of the probability current of reactive trajectories can also be defined as the ensemble of solutions of [compare (10)]

$$\frac{dx_i(\tau)}{d\tau} = \mathcal{J}_{AB,i}^x(x(\tau),v(\tau)),$$

$$\tag{20}$$

$$\frac{dv_i(\tau)}{d\tau} = \mathcal{J}_{AB,i}^v(x(\tau),v(\tau)),$$

and they can be used to define reaction tubes carrying a given percentage of the probability flux of reactive trajectories as in the overdamped case.

Finally, the committor function $q(x,v)$ satisfies the backward Kolmogorov equation associated with (13) [compare (12)],

$$0 = \sum_{i=1}^n \left(v_i\frac{\partial q(x,v)}{\partial x_i} - m_i^{-1}\frac{\partial V(x)}{\partial x_i}\frac{\partial q(x,v)}{\partial v_i} + m_i^{-1}\gamma_i v_i\frac{\partial q(x,v)}{\partial v_i}\right.$$

$$\left. + k_BTm_i^{-1}\gamma_i\frac{\partial^2 q(x,v)}{\partial v_i^2}\right),$$

$$\tag{21}$$

$$q(x,v)|_{(x,v)\in\partial\mathcal{A}} = 0, \quad q(x,v)|_{(x,v)\in\partial\mathcal{B}} = 1.$$

The only additional difficulty with (21) absent with (12) is that, because the differential operator in (21) is degenerate (i.e., hypoelliptic but not elliptic), in order to be able to impose the Dirichlet boundary conditions on $\partial\mathcal{A}$ and $\partial\mathcal{B}$, the unit normal to these sets at (x,v) must span the velocity degrees of freedom everywhere except maybe on a set of zero measure on $\partial\mathcal{A}$ and $\partial\mathcal{B}$. How to solve (21) in the context of the simple example considered in Sec. VII is briefly discussed in Sec. II C.

C. Numerical aspects

Here we briefly discuss how we did the numerics on the examples discussed below. In order to get an accurate approximation of the committor functions $q(x)$ and $q(x,v)$, we derived a stable finite differences scheme for the discretization of (12) and (21) and implemented the resulting scheme

in MATLAB. In all numerical computations involving (12) we choose a rectangular domain $\Omega \subset \mathbb{R}^2$ and a uniform mesh. The Dirichlet conditions for $q(x)$ are included into our scheme by defining discrete sets A and B via the mesh. We also added a Neumann boundary condition on the boundary of the domain, $\partial_{\hat{n}} q(x)|_{\partial \Omega} = 0$. The same procedure was applied to solve (21), except that the grid was rotated by $\pi/4$ to ensure numerical stability. Since the intention of this paper is to illustrate the TPT for simple examples rather than presenting the details of the numerics, we refer the reader to a second paper[23] for a detailed presentation of our scheme which includes the discussion of its stability and accuracy.

To compare and test the predictions of TPT, we also computed some of the statistical quantities provided by TPT by means of direct numerical simulation (DNS) of the dynamical equations (1) and (13). As explained earlier, an ensemble of reactive trajectories can be computed by pruning a sufficiently long trajectory. This was done by discretizing (1) and (13) in such a way that long-term stability is achieved. The results presented below are based on the Euler-Maruyama scheme for the overdamped dynamics and an appropriate second order scheme for the Langevin dynamics[24] which both have been used with sufficiently small discretization time steps to guarantee stability.

From the long trajectory generated by DNS, the committor function was obtained by binning the region between the reactant and product state and computing the ratio between the time spend by the reactive trajectories in each bin and the total time the long trajectory was reactive. The reaction rate was obtained by counting the number N of transitions from A to B in the long trajectory of length T and dividing this number by T. It should be stressed that the trajectory must be extremely long in order to obtain a statistically accurate estimate of $q(x)$, $q(x,v)$, and k_{AB} by DNS, which makes the DNS much more expensive than the numerical solution of (12) and (21). In what follows, T denotes the length of the trajectory and N the number of reactive pieces within.

III. DIFFUSION IN THE DOUBLE-WELL POTENTIAL

For our first example, we choose the two-dimensional potential [here and below we denote $(x,y)=(x_1,x_2)$],

$$V(x,y) = \tfrac{5}{2}(x^2 - 1)^2 + 5y^2, \tag{22}$$

which is a combination of a double-well potential in x direction and a harmonic potential in y direction. The local minima at $(-1,0)$ and $(0, 1)$ are separated by a saddle point at $(0, 0)$. We choose the inverse temperature $\beta = 1$ such that the process spends the most of its time within the two wells, and we also set $\gamma_x = \gamma_y = 1$. The equilibrium distribution of the overdamped dynamics (1) associated with (22) is depicted in Fig. 2.

For the reactant and product states, A and B, we choose the two neighborhoods of the two minima of the potential at $(-1,0)$ and $(1, 0)$ such that they include all states x that satisfy $V(x,y) < 0.4$; as in all subsequent computations these sets are replaced by the sets of all grid points satisfying this condition. We also restricted the computation to the domain $\Omega = [-1.5, 1.5] \times [-1, 1]$, which is large enough so that the
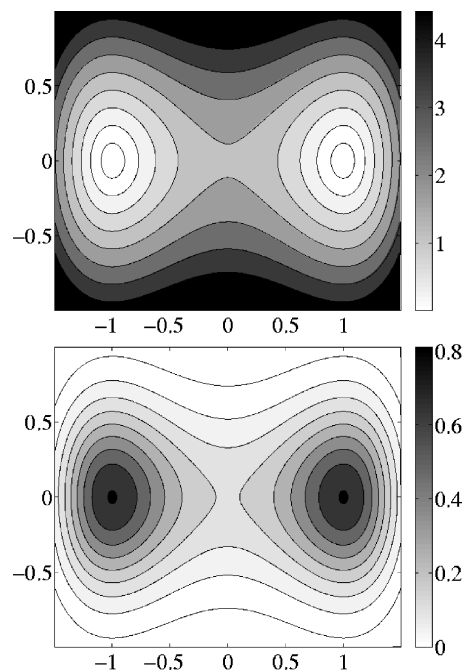

FIG. 2. Upper: Contour plot of the double-well potential. Lower: Contour plot of the Boltzmann-Gibbs probability density function $Z^{-1}e^{-\beta V(x,y)}$. Results for $\beta = 1$. The regions around the minima at $(-1,0)$ and $(1,0)$ contain most of the probability, i.e., they are metastable.

potential is high at the boundaries (and hence the Boltzmann-Gibbs probability density is very small there). To discretize Ω, we used a uniform grid consisting of 500×500 grid points.

A. Committor function

Figure 3 shows the level sets (isolines) of the committor function $q(x,y)$ obtained by solving (12) for this example. The left-right symmetry of the level sets of $q(x,y)$ with respect to the piece of the vertical axis $S = \{(0,y) | -1 \leq y \leq 1\}$ which includes the saddle point $(0, 0)$ is a consequence of the choice of domain Ω, the symmetry of the potential (22), and the symmetry between A and B. In particular, it is clear that the probability to reach A before B should be $\frac{1}{2}$ for all points on S, i.e., $q(0,y) = \frac{1}{2}$ for all $-1 \leq y \leq 1$. This prediction is confirmed by the numerics.
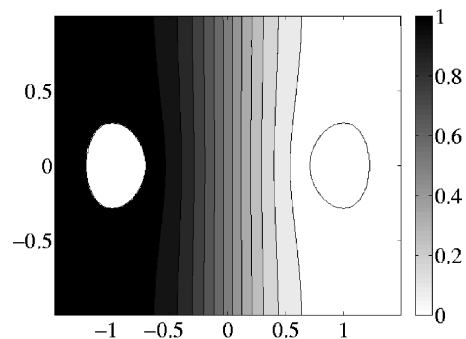

FIG. 3. Contour plot of the committor function $q(x,y)$ solution of (12) at inverse temperature $\beta = 1$. The white regions are the reactant state A and product state B (A is the right, B at the left). The level sets (isolines) of $q(x,y)$ are the regions from which the probability to reach first A rather B is uniform.
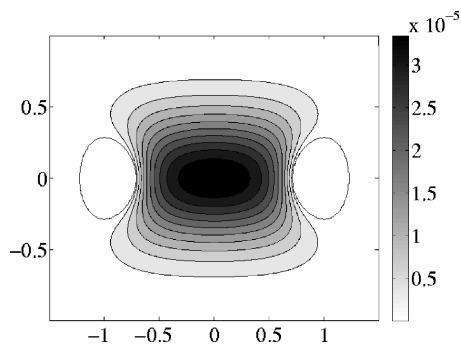
FIG. 4. Contour plot of the probability density function $\rho_{AB}(x,y)$ of reactive trajectories obtained via (5). Results for $\beta=1$.

B. Probability density function of reactive trajectories

Knowing $q(x,y)$ we can compute the probability density function of reactive trajectories $\rho_{AB}(x,y)$ via (5). This probability density function is shown in Fig. 4. The density $\rho_{AB}(x,y)$ is peaked around the saddle point (0, 0) which indicates that the region around the saddle point is the dynamical bottleneck (transition state region) for the reaction.

For comparison, the probability density function of reactive trajectories $\rho_{AB}(x,y)$ was also computed by DNS. In the upper picture of Fig. 5 a typical reactive trajectory is shown. In the lower panel of Fig. 5 the probability density function of reactive trajectories as computed via DNS is shown. The result of DNS agrees with the prediction of TPT shown in Fig. 4. Notice, however, that the probability density $\rho_{AB}(x,y)$ obtained by DNS is subject to significantly larger errors of statistical origin.
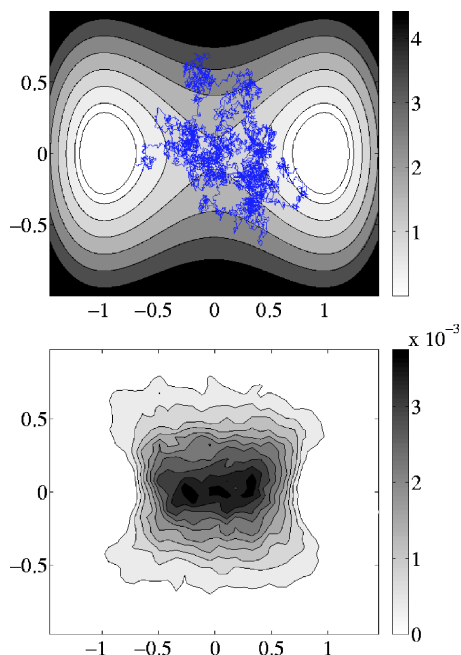

FIG. 5. Upper: A typical reactive trajectory. Lower: Probability density function of reactive trajectories computed via DNS based on 300 reactive trajectories and represented on a 40×40 box discretization of the domain Ω. Results for $\beta=1$.
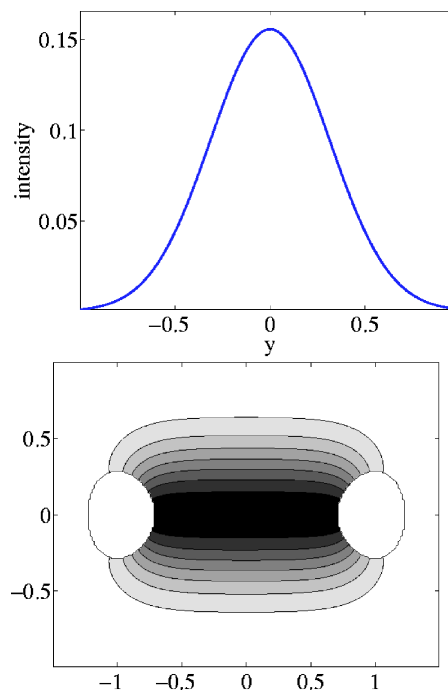

FIG. 6. Upper: Intensity of the probability current of reactive trajectories on the isocommittor surface $S_{1/2}=\{(x,y):q(x,y)=0.5\}=\{(0,y):-1 \leqslant y \leqslant 1\}$. Lower: Streamlines of the probability current $J_{AB}(x,y)$ colored according to the intensity of the current on the isocommittor surface $S_{1/2}$. Results for $\beta=1$. The darker the color, the higher the intensity of the probability current of reactive trajectories through this region.

C. Probability current of reactive trajectories and its streamlines

Knowing $q(x,y)$, we can also compute the probability current of reactive trajectories via (6) and its streamlines via (10). These streamlines are shown in the lower picture of Fig. 6.

In order to better visualize the probability current as well as the reaction tubes mentioned in Sec. II, we did the following: First we computed the intensity of the probability current on a dividing surface of interest, for which we choose the isocommittor $\frac{1}{2}$ surface, $S_{1/2}=\{(x,y):q(x,y)=\frac{1}{2}\}$. Since the isocommittor surface $S_{1/2}$ is simply the piece of the y axis in Ω, the intensity $J_{AB} \cdot \hat{n}_{S_{1/2}}$ of the probability current on $S_{1/2}$ can be expressed by

$$J_{AB,1}(0,y) = k_B T Z^{-1} e^{-\beta V(0,y)} \frac{\partial q(0,y)}{\partial x}. \tag{23}$$

This intensity on $S_{1/2}$ is shown in the upper picture of Fig. 6. We observe that the intensity of the current is maximum at $(0,y)=(0,0)$ which corresponds to the saddle point. This means that most reactive trajectories cross $S_{1/2}$ near the saddle point or, equivalently, that the probability flux of reactive trajectories across $S_{1/2}$ is concentrated near the saddle point.

Next, from each point $(0,y)$ on $S_{1/2}$ we transported the value of the current intensity $J_{AB}(0,y)$ backwards and forwards along each streamline of the current $J_{AB}(x,y)$ until it enters the states A and B. With this procedure, we give each point along a streamline the value of the current intensity evaluated at the point on $S_{1/2}$ through which the streamline

TABLE I. Reaction rate computed for the double-well potential for $\beta=1$. The rate predicted by TPT is consistent with the rate computed via DNS (out of $N=10^5$ reactive trajectories). The error given on the rate computed via DNS is the estimated statistical error. There is an additional error (not given) on all rates due to discretization of the domain; this error can be estimated from the difference between the rates obtained via (24) and via (25).

k_{AB} via (24)	1.225×10^{-1}
k_{AB} via (25)	1.226×10^{-1}
k_{AB} via DNS	$(1.230 \pm 0.029) \times 10^{-1}$

goes. This is how the coloring in the lower picture of Fig. 6 was obtained: the darker the region, the higher the current intensity is. Regions in this figure which include all the grays down to a certain level form reactions tubes carrying a given percentage of the probability flux of reactive trajectories (the lower the level of gray, the higher the percentage; in this example, the tube in black already carries 42% of the flux).

D. Reaction rate

Now we turn our attention to the reaction rate k_{AB}. Choosing $S_{1/2}$ as dividing surface in (8), this expression for the reaction rate reduces to

$$k_{AB} = \beta^{-1} Z^{-1} \int_{-1}^{1} e^{-\beta V(0,y)} \frac{\partial q(0,y)}{\partial x} dy. \qquad (24)$$

Alternatively, we can compute k_{AB} via (9),

$$k_{AB} = k_B T Z^{-1} \int_{\Omega_{AB}} \left(\left(\frac{\partial q(x,y)}{\partial x} \right)^2 + \left(\frac{\partial q(x,y)}{\partial y} \right)^2 \right)$$
$$\times e^{-\beta V(x,y)} dx dy. \qquad (25)$$

We approximate the partial derivatives $\partial q / \partial x$ and $\partial q / \partial y$ which are involved in both expressions for the rate on the mesh used to compute the committor function.

We compare the rate k_{AB} computed via DNS with the rates obtained from (24) and (25). Table I shows that the agreement of all different results is very good.

IV. ENTROPIC BARRIERS: PURE DIFFUSION

In our next example we consider pure diffusion in a square $\Omega = [0,1] \times [0,1]$ with two obstacles such that the domain becomes the S-shaped region shown in Fig. 7. By pure diffusion we mean that we consider the overdamped dynamics in a flat potential, $V(x,y)=0$ in (1), except for the presence of hard walls at the boundary of the domain. We are interested in the statistics of the reactive trajectories starting in a region near the upper-right corner and ending in a region near the bottom-left corner and define the reactant and product states A and B accordingly (see Fig. 7). In contrast with the previous example where the transition between A and B is constrained by a potential barrier, here the dynamics has to overcome an *entropic barrier*: it has to find its way between the two obstacles. Suppose we start the dynamics in A. The closer the dynamics gets to the region enclosed by the obstacles the higher the probability that the dynamics will finally reach the left-down corner before returning to A because the probability to end up in B depends only on the
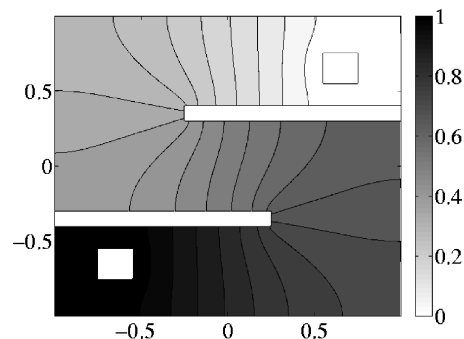

FIG. 7. Contour plot of the committor function $q(x,y)$ for the pure diffusion in the S-shaped domain. The reactant state A and product state B are the two squares in the upper-right and bottom-left corners, respectively. The two thin white rectangular regions connecting to the vertical sides of the domain are hard walls. Results for $\beta=1$. In this example, the Boltzmann-Gibbs probability density $Z^{-1}e^{-\beta V(x,y)}$ is uniform in the domain since $V(x,y)=0$ except at the walls where it is infinity.

distance between the current position and the set B. Figure 7 shows the committor function $q(x,y)$ as computed for this example; its isolines nicely illustrate the particular behavior of the dynamics.

From the symmetry of the domain $\Omega \setminus (A \cup B)$ it is clear that the committor goes through the point $(0,0)$. Therefore it is very likely to encounter a reactive trajectory between the obstacles, in the vicinity of the committor. In the upper picture of Fig. 8 we depict a typical reactive trajectory. One can see that the reactive trajectory spends most of its time between the obstacles. This is also obvious from the contour plot of the probability density function of reactive trajectories $\rho_{AB}(x,y)$ shown in the lower panel of Fig. 8. Notice how complicated the reactive trajectory is in this example and how much simpler $\rho_{AB}(x,y)$ is. The probability current of
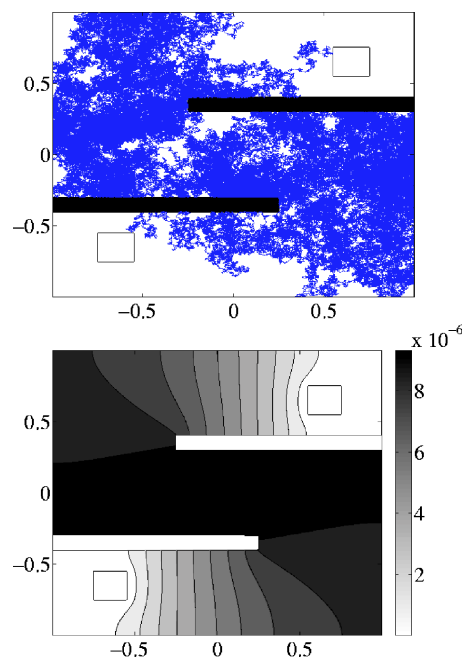

FIG. 8. Upper: A typical reactive trajectory. Lower: Contour plot of the probability density function of reactive trajectories $\rho_{AB}(x,y)$. Results for $\beta=1$.

TABLE II. The reaction rate k_{AB} for the pure diffusion in the S-shaped domain. Results for $\beta = 1$ and $N = 10^5$ in the DNS.

Rate via (8)	4.455×10^{-2}
Rate via (9)	4.443×10^{-2}
Rate via DNS	$(4.425 \pm 0.144) \times 10^{-2}$

reactive trajectories (not shown) can also be computed in this example but it turns out to be very simple (basically, the streamlines follow the S shape).

In order to complete our observation for this example, Table II gives the values of the transition rates computed via TPT and via DNS. Again the values agree within numerical accuracy.

This example clearly shows that TPT is not restricted to situations in which the reaction pathway is determined by energy effects, as in the example in Sec. III, but it also allows one to handle situations where entropic effects dominate.

V. ENTROPIC SWITCHING: DIFFUSION IN A THREE-HOLE POTENTIAL

In the next example, we study an example with two different reaction channels. For this purpose, we choose the three-hole potential,

$$V(x,y) = 3e^{-x^2 - \left(y - \frac{1}{3}\right)^2} - 3e^{-x^2 - \left(y - \frac{5}{3}\right)^2} - 5e^{-(x-1)^2 - y^2}$$
$$- 5e^{-(x+1)^2 - y^2} + 0.2x^4 + 0.2\left(y - \frac{1}{3}\right)^4, \qquad (26)$$

which has been already considered in. Refs. 21 and 27.

As one can see in the upper picture of Fig. 9 the potential (26) has two deep minima approximately at $(\pm 1, 0)$, a shallow minimum approximately at $(0, 1.5)$, three saddle points approximately at $(\pm 0.6, 1.1)$, $(-1.4, 0)$, and a maximum at $(0, 0.5)$. Thus, the two deep minima are connected by
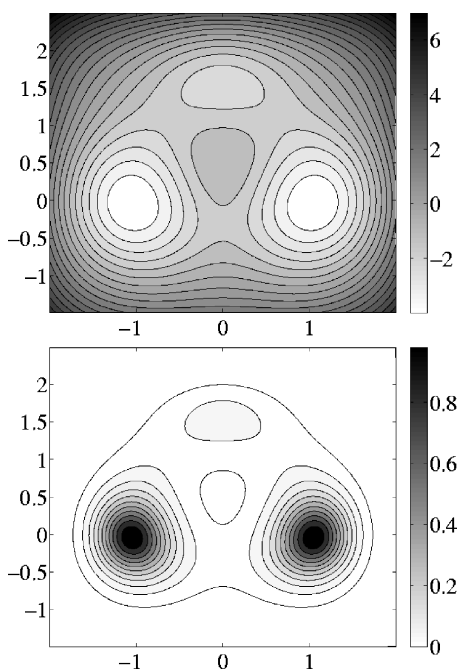

FIG. 9. Upper: Contour plot of the three-hole potential. Lower: Contour plot of the Boltzmann-Gibbs probability density function $Z^{-1}e^{-\beta V(x,y)}$ at $\beta = 1.67$.
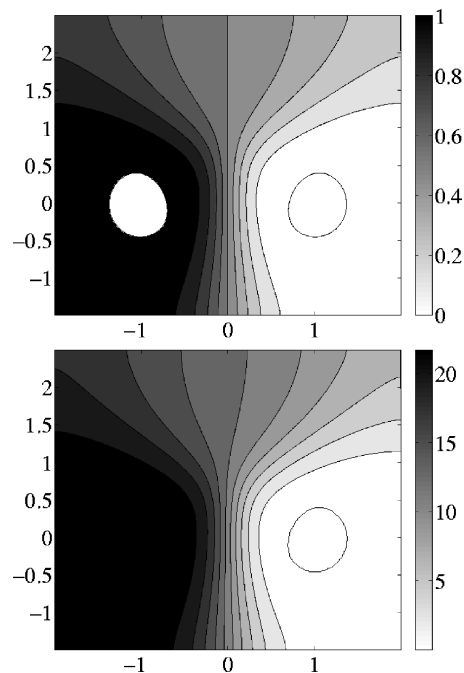

FIG. 10. Upper: Contour plot of the committor function $q(x,y)$ at $\beta = 1.67$. Lower: Contour plot of the MFPT with respect to the set A as also analyzed in Ref. 21.

an upper and a lower channel, and the upper channel contains the additional, less-pronounced minimum. The dynamical bottlenecks in the upper channel are the two saddle points with equal potential energy whereas the dynamics in the lower channel has only to overcome one saddle point whose potential energy is higher compared to the other two. It is known from large deviation theory[25] that in the limit $\beta \to \infty$ the reaction will occur via the upper channel with probability 1 since the energy barrier is lower there. Therefore we expect that the dynamics prefers the upper channel at low (finite) temperature. At higher temperature, however, the lower channel should be preferred (since it is direct). This entropic switching effect was first discovered and analyzed in Ref. 21. There the authors used the gradient of the mean first passage time (MFPT) with respect to a given state to detect the transition channels and their dependence of the temperature.

In this example, we performed experiments at two inverse temperature: $\beta = 6.67$ (low temperature), which is such that the upper channel is the preferred reaction tube, and $\beta = 1.67$ (high temperature), which is such that the lower channel is the preferred reaction tube.

In the upper picture of Fig. 10 we show the contour plot of the committor function at $\beta = 1.67$. As in the previous examples the symmetry of the domain Ω_{AB} explains that the isocommittor surface $\frac{1}{2}$ is $S_{1/2} = \{(0, y) : -2 \le y \le 2\}$. Notice how the presence of the shallow minima in the upper channel spreads the level sets of $q(x,y)$ in this region. This follows from the fact that the reactive trajectories going through the upper channel get trapped in the shallow well for a long period of time before exiting towards the set B. Notice that it also implies that the isocommittor $\frac{1}{2}$ surface goes through the shallow minima and not through one of the two upper saddle points. The committor function at $\beta = 6.67$ (not shown) is
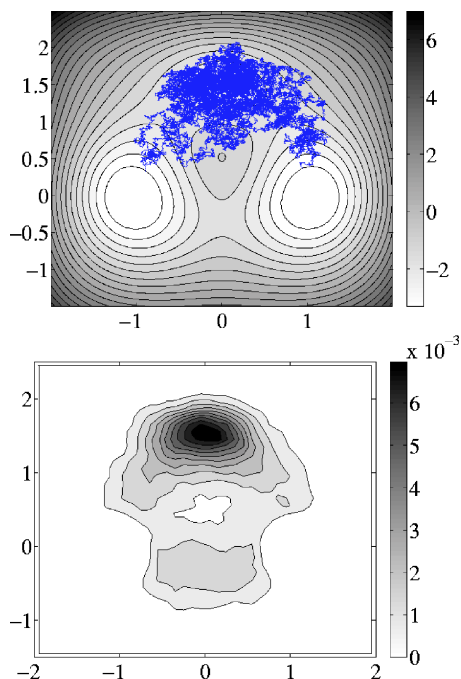
FIG. 11. Upper: A typical reactive trajectory at a high temperature $\beta=1.67$ taking the upper channel with the two saddle points with lowest energy. Lower: Contour plot of the probability density function of reactive trajectories computed via DNS at $\beta=1.67$ from 500 reactive trajectories using a 40×40 box discretization of the domain $\Omega=[-2,2]\times[-1.5,1.5]$.

very similar to the one at $\beta=1.67$ (though, as we will see below, the probability density function and the probability current of reactive trajectories are very different). The lower picture of Fig. 10 illustrates the similarity between reaction coordinate and MFPT with respect to the set A. This similarity is a specialty of this example and will not be guaranteed in general.

Now we turn our attention to the probability density function of reactive trajectories $\rho_{AB}(x,y)$ for this example. The pictures in Fig. 11 illustrate this situation for $\beta=1.67$ (high temperature) as computed via DNS. In Fig. 12 we depict the probability density function of reactive trajectories from TPT computed at two different temperatures. The upper picture shows the density for a low temperature ($\beta=6.67$) and the lower one for a high temperature ($\beta=1.67$). The first observation is that both densities attain their maximum in the shallow minima. This is because the shallow minima catch the dynamics on its way from A to B. As a consequence, the reactive trajectories spend a long time within this region and therefore the probability to encounter a reactive trajectory there increases. However, one can see that at high temperature there is a certain probability to encounter a reactive trajectory in the lower channel. But which reaction channel does the dynamics prefer depending on the temperature? From the viewpoint of the density $\rho_{AB}(x,y)$ we cannot answer this question since the long residency of reactive trajectories in the vicinity of the shallow minima spoils the information about the relative *number* of reactive trajectories going there.

To answer the question of which reaction channel is preferred at different temperatures we must consider the probability current of reactive trajectories $J_{AB}(x,y)$. In Fig. 13 we
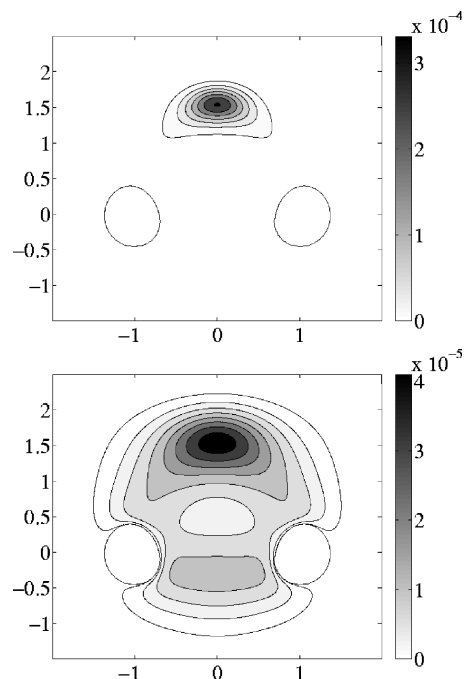

FIG. 12. Contour plots of the density $\rho_{AB}(x,y)$ for two different temperatures. Upper: low temperature $\beta=6.67$; Lower: high temperature $\beta=1.67$. In both cases $\rho_{AB}(x,y)$ attains its maximum in the shallow minima.

show the transition tubes computed via its streamlines with colors induced by the intensity of the probability current on the isocommittor surface $\frac{1}{2}$, using the procedure explained in Sec. III C. One can clearly see that the transition tubes give the desired information. At the low temperature (upper pic-
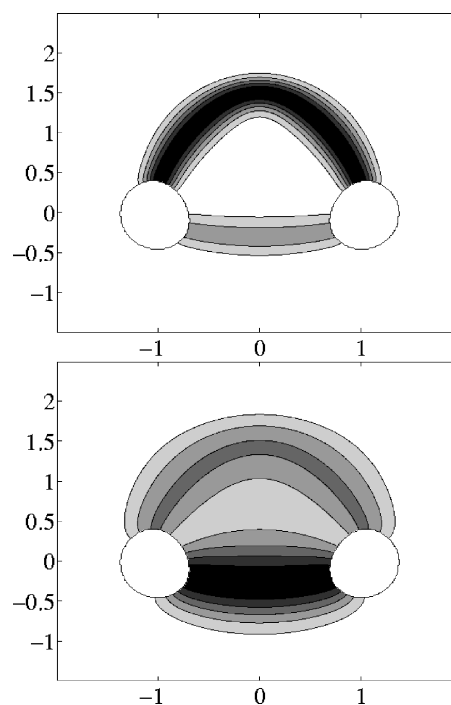

FIG. 13. Streamlines of the probability current of reactive trajectories colored according to the intensities of the probability current on the isocommittor $\frac{1}{2}$ surface for two different temperatures. Upper: At the low temperature $\beta=6.67$ the upper channel is the preferred reaction channel. Lower: At the high temperature $\beta=1.67$ most of the reactive trajectories take the lower channel.

TABLE III. Reaction rates for the three-hole potential for $\beta=6.67$ and $\beta=1.67$. One can see that for $\beta=1.67$ the rate computed via DNS ($N=10^5$) is consistent with those predicted from TPT. For $\beta=6.67$ the rate is so small that any computation via DNS would lead to totally unreasonable effort (to obtain $N=10^5$ reactive trajectories, it would require to generate a long trajectory of length $T \approx 10^5/k_{AB}=10^{12}$). The computations via finite difference discretization of (12) take only a few seconds on a standard personal computer (PC).

	$\beta=6.67$	$\beta=1.67$
Rate via (8)	9.47×10^{-8}	1.912×10^{-2}
Rate via (9)	9.22×10^{-8}	1.924×10^{-2}
Rate via DNS		$(1.918 \pm 0.052) \times 10^{-2}$

ture) the preferred transition channel is the upper one and at the high temperature (lower picture) it is the lower one. This result is consistent with observations made in Ref. 21. We complete this example by stating the reaction rate for the two temperatures in Table III. As in the previous examples we choose the isocommittor surface $\frac{1}{2}$ for the rate computations via (24).

This example shows that TPT is able to handle situations with multiple reaction channels, possibly with intermediate metastable states along them, and can distinguish which channel is preferred depending on the temperature (entropic switching). It also shows that all the object provided by TPT—the probability density of the reactive trajectories, their probability current and the associated streamlines—are necessary (and sufficient) to understand the mechanism of the reaction, while $\rho_{AB}(x,y)$ alone is not.

VI. DIFFERENT TIME SCALES: FAST-SLOW DIFFUSION IN A DOUBLE-WELL POTENTIAL

In the last example for the overdamped dynamics we consider a diffusion process with two variables subject to different friction coefficients leading to two different time scales. For this purpose we consider a process generated by

$$\dot{x}(t) = -\frac{\partial V(x(t),y(t))}{\partial x} + \sqrt{2k_B T}\,\eta_x(t),$$

$$\epsilon \dot{y}(t) = -\frac{\partial V(x(t),y(t))}{\partial y} + \sqrt{2k_B T \epsilon}\,\eta_y(t). \qquad (27)$$

This system is a special case of (1) with $\gamma_x=1$ and $\gamma_y \equiv \epsilon > 0$. For $\epsilon \ll 1$, the variable y is fast compared to x. For details see Ref. 26. Despite the different time scales, the equilibrium distribution is still given by the Boltzmann-Gibbs density $Z^{-1}e^{-\beta V(x,y)}$ for every value of $\epsilon > 0$. For the potential V, we choose a double-well potential in y direction which is coupled to a harmonic potential in x direction,

$$V(x,y) = 5(y^2-1)^2 + 1.25\left(y - \tfrac{1}{2}x\right)^2. \qquad (28)$$

The potential attains two local minima at $(-2,-1)$ and $(2,1)$ which are separated by a saddle point at $(0,0)$. For our computations we choose $\epsilon=0.1$, so that the dynamics in the y direction is roughly ten times faster than in the x direction. The potential energy surface is shown in Fig. 14 together with equilibrium probability density function for $\beta=1$. The
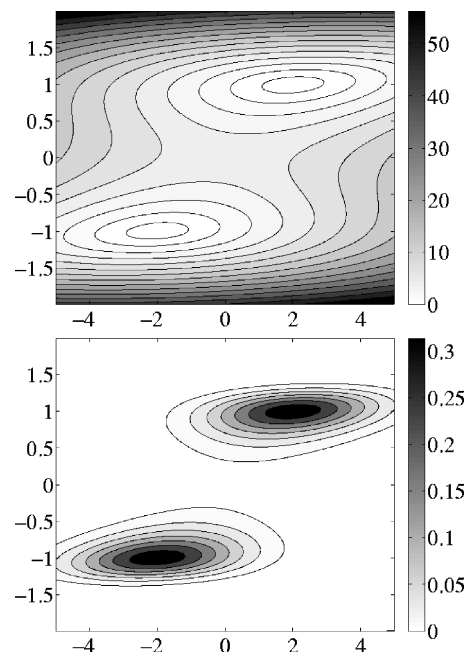

FIG. 14. Upper: Contour plot of the potential (28). Lower: Contour plot of Boltzmann-Gibbs equilibrium probability density function. Results for $\beta=1$.

key for understanding of the reaction is to realize that the important barriers for the dynamics are the barriers in the y direction. Suppose we fix an $x=x_0$ and consider the restricted potential $V(x_0,y)$, which then only depends on y. Due to the separation of time scale, this is the potential that the y variable effectively feels while the x variable is quasifrozen and evolving only on a longer time scale. Consider the energy barriers for different x_0 in $V(x_0,y)$; denoting these barriers by $\Delta V(x_0)$, it can be seen that $\Delta V(x_0)$ attains a local maximum at $x_0=0$ and decreases as $|x_0|$ increases which is illustrated in Fig. 15. Because of this feature, one expects that the reactive trajectories will tend to wait near the reactant state A until they reach a fiber in the y direction with a low barrier $\Delta V(x_0)$ to hop over. Since there are two groups of such fibers on either side of the y axis, there should be two predominantly vertical reaction channels. Let us now confirm this intuitive picture via TPT.

The contour plot of the isocommittor function is shown in Fig. 16. Consistent with the separation of time scale it shows that the isocommittor surfaces are predominantly ver-
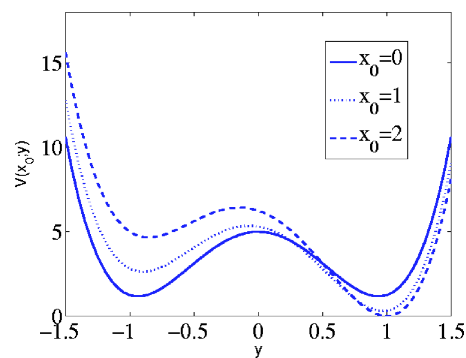

FIG. 15. The potential $V(x_0,y)$ of the fast-slow example as a function of y for $x_0=0$, $x_0=1$, and $x_2=2$.
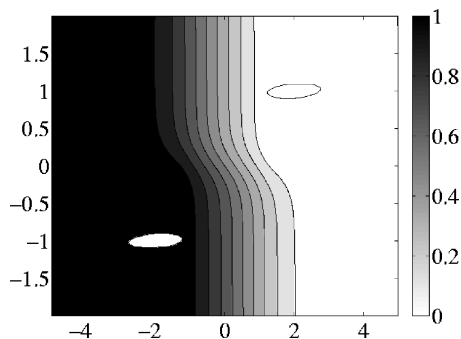
FIG. 16. Contour plot of the isocommittor function for the fast-slow example with $\beta=1$ and $\epsilon=0.1$.

tical except in a narrow strip around the x axis. A typical reactive trajectory is shown in the upper picture of Fig. 17. Consistent with the intuitive picture given above, because of the separation of time scale, the trajectory spends a relatively long amount of time in the vicinity of the states A and B and a relatively short amount of time transiting between these states (the latter motion being predominantly in the fast y direction). As explained in the previous example, this behavior of the dynamics affects the probability density function of the reactive trajectories which is peaked in the regions where the trajectories spend most time. The lower picture of Fig. 17 shows this effect. The probability density function $\rho_{AB}(x)$ is bimodal and attains local maxima in regions close to the states A and B. Notice that $\rho_{AB}(x)$ does not give much information about the reaction channels. To visualize the reaction channels we proceed similarly as in the previous examples and choose the dividing surface $S=\{(x,0):-1.5\leqslant x\leqslant 1.5\}$ to compute the intensity of the probability current used to color the streamlines of this current. The results are shown in Fig. 18. Consistent with the intuitive picture given above, there are two predominantly vertical channels. Notice that most of
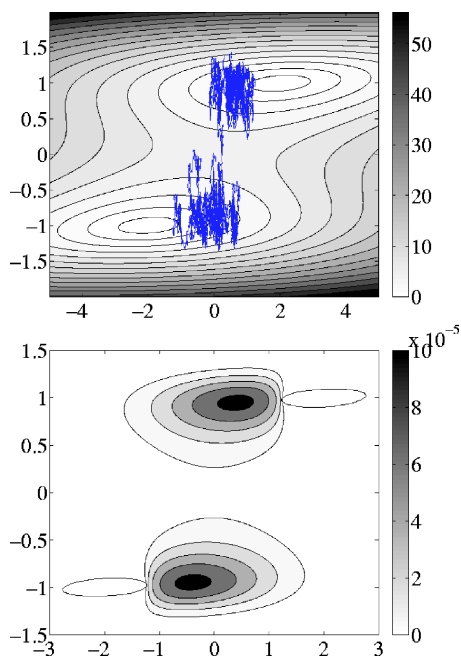

FIG. 17. Upper: Typical reactive trajectories in (27). Lower: Probability density function of reactive trajectories. Results for $\beta=1$ and $\epsilon=0.1$.
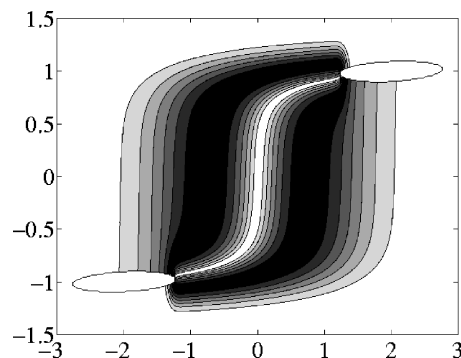

FIG. 18. Streamlines of the probability current colored according to the intensities on the dividing surface $S=\{(x,0):-1.5\leqslant x\leqslant 1.5\}$. Result for $\beta=1$.

the flux across S goes either at the left or the right of the saddle point. Finally, the reaction rate predicted by TPT and computed by DNS is given in Table IV.

This example illustrates the subtle effects that time-scale separation may have on the reaction pathway and shows that TPT is able to capture these effects.

VII. LANGEVIN DYNAMICS

In this section we apply TPT to an example of the Langevin equation (13). Here we assume that $(x,v)\in\mathbb{R}\times\mathbb{R}$ (one degree of freedom) and we set $\gamma=m=1$. We also assume that the potential is the double-well potential given by

$$V(x)=(x^2-1)^2,$$

with minima at $x=-1$ and $x=1$ and a local maxima at $x=0$. In Fig. 19 we show the associated Hamiltonian $H(x,v)$ and the Boltzmann-Gibbs equilibrium probability density function for $\beta=1$. Although the structure of the potential is very simple, it allows us to illustrate how the reaction pathway depends on the friction constant γ. Keeping the temperature constant, we study three different scenarios: the high, medium, and low friction cases. For reason of numerical stability we have to introduce a coordinate transformation which amounts to rotate the grid by $\pi/4$ and solve the committor equation (21) on this grid (see Ref. 23). This explains our unusual choice of the diamond-shaped domain Ω as visible in Fig. 19. The reactant state $\mathcal{A}$ and the product state $\mathcal{B}$ are determined in a similar way as in the previous section, i.e., their union include all states (x,v) with $H(x,v)<1$.

Before we start with a detailed description of the reaction pathways, we state the reaction rates in Table V computed for different friction coefficients via TPT and compare them with those obtained via direct numerical simulation of the Langevin dynamics (13). As one can see in Table V the rates agree within numerical error.

TABLE IV. Reaction rate computed for the fast-slow potential at $\beta=1$. Results of DNS based on $N=10^5$ reactive trajectories.

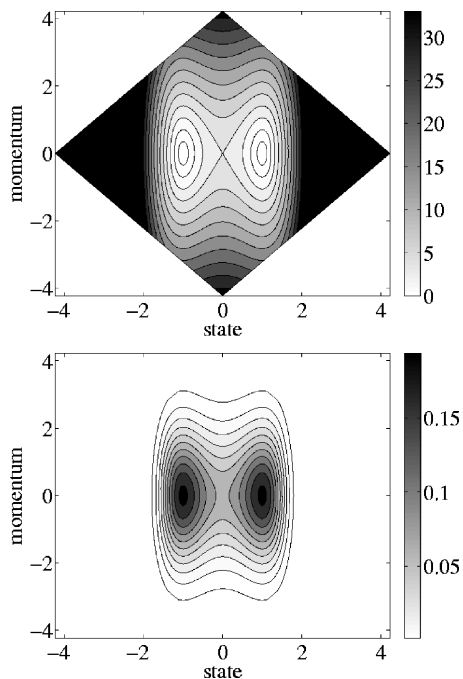|	
k_{AB} via (18)	3.278×10^{-2}
k_{AB} via (19)	3.239×10^{-2}
k_{AB} via DNS	$(3.189\pm0.076)\times10^{-2}$

FIG. 19. Upper: Contour plot of the Hamiltonian $H(x,v)$. Lower: Contour plot of the Boltzmann-Gibbs equilibrium probability density function $\mathcal{Z}^{-1}e^{-\beta H(x,v)}$. Results for $\beta=1$.

A. High friction case, $\gamma=10$

As mentioned in Sec. II, Langevin leads to overdamped dynamics in the high friction limit $\gamma\rightarrow\infty$. In the present case, the overdamped equation is the one-dimensional equation,

$$\gamma\dot{x}(t)=4(x(t)-x^3(t))+\sqrt{2k_BT\gamma}\eta(t). \tag{29}$$

Since (29) involves the position $x(t)$ but not the velocity $v(t)$, in this limit the probability to reach the set $\mathcal{B}$ before the set $\mathcal{A}$ conditioned on starting at point (x_0,v_0) must be independent of the velocity v_0. In other words, for large enough γ, $q(x,v)\approx q(x)$ where $q(x)$ is the committor function of (29) and the level sets of the committor function are (almost) parallel to the velocity axis. This is confirmed by the results shown in Fig. 20. The little deviations near the upper and lower corners are due to the Neumann boundary condition which forces the level sets of the committor function to be perpendicular to the boundaries. Notice that $q(x,v)\approx q(x)$ also implies that $q_b(x,v)\approx 1-q(x)$. This is also confirmed by the results shown in Fig. 20. The upper picture of Fig. 21 is a contour plot of the probability density function of reactive trajectories $\varrho_{\mathcal{AB}}(x,v)$. This density is peaked around the saddle point of the Hamilton function $H(x,v)$ at

TABLE V. Reaction rates computed for several friction coefficients via DNS of the Langevin dynamics and via TPT using (19) or (18). All computations are done for the same temperature $\beta=1$.

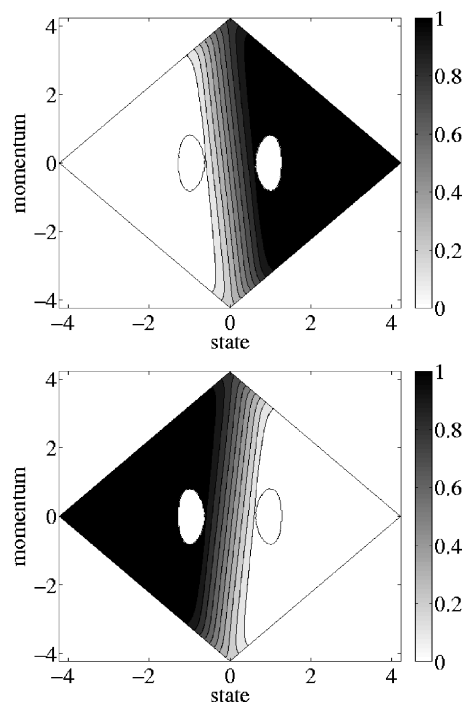|	k_{AB} via DNS	k_{AB} via (19)	k_{AB} via (18)
$\gamma=1$	$(3.833\pm0.061)\times10^{-2}$	3.778×10^{-2}	3.721×10^{-2}
$\gamma=2$	$(4.019\pm0.171)\times10^{-2}$	3.918×10^{-2}	3.898×10^{-2}
$\gamma=5$	$(2.634\pm0.106)\times10^{-2}$	2.523×10^{-2}	2.483×10^{-2}
$\gamma=10$	$(1.534\pm0.032)\times10^{-2}$	1.460×10^{-2}	1.361×10^{-2}

FIG. 20. Upper: Contour plot of the committor function $q(x,v)$. Lower: Contour plot of the backward committor function $q_b(x,v)=1-q(x,-v)$. Results for $\beta=1$, $\gamma=10$.

$(x,v)=(0,0)$ and only shows a slight up-down asymmetry, consistent with the velocity playing no role in the mechanism of the reaction. In the lower picture of Fig. 21 we show the streamlines of the probability current (17) of reactive trajectories colored as in the previous example in function of the intensity of the current on $S=\{(0,v):-3\leqslant v\leqslant 3\}$. The reaction channel is predominantly horizontal.
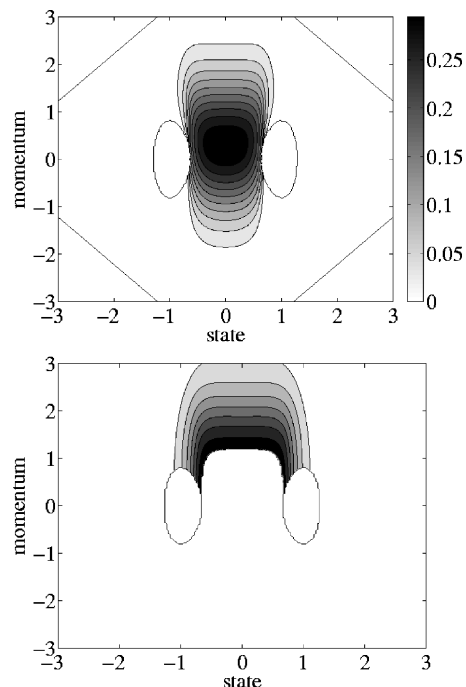

FIG. 21. Upper: Probability density function of reactive trajectories $\varrho_{\mathcal{AB}}(x,v)$. Lower: Reaction tube based on streamlines of the probability current colored according to the intensity of the probability current on the dividing surface $S=\{(0,v):-3\leqslant v\leqslant 3\}$. Results for $\beta=1$, $\gamma=10$.
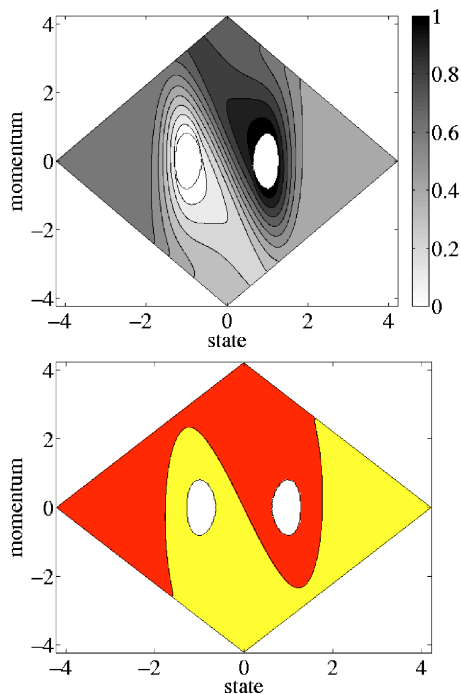
FIG. 22. Upper: Contour plot of the committor function $q(x,v)$ for $\beta=1$, $\gamma=1$. Lower: Decomposition of the domain Ω in phase space into the two regions $\{(x,v):q(x,v)<0.5\}$ (light gray) and $\{(x,v):q(x,v)>0.5\}$ (dark gray). The dividing curve is the isocommittor $\frac{1}{2}$ surface where $q(x,v)=\frac{1}{2}$.

B. Medium friction case, $\gamma=1$

In the medium friction case, the reaction pathway changes dramatically and now involve the velocity as well as the position. This is apparent from the contour plot of the committor function $q(x,v)$ shown in the upper picture of Fig. 22 and the partition of the domain by the isocommittor $\frac{1}{2}$ surface shown in the lower picture. Clearly, the committor function $q(x,v)$ now depends crucially on the velocity, unlike in the high friction case. In fact, the partition of the domain by the isocommittor $\frac{1}{2}$ surface is simple to understand: it is the ghost of the partition of the domain by the deterministic dynamics,

$$\dot{x}(t)=v(t),$$

$$(30)$$

$$\dot{v}(t)=-\frac{\partial V(x(t))}{\partial x}-\gamma v(t).$$

Because $\gamma>0$ in this equation, every trajectory initiated at a point $(x,v)\in\mathbb{R}^n\times\mathbb{R}^n\setminus(\mathcal{A}\cup\mathcal{B})$ will asymptotically end up either in state $\mathcal{A}$ or in state $\mathcal{B}$. Figure 23 shows the partition of phase space that this induces: the dark gray region contains all the points which end up in $\mathcal{B}$ and the light gray region those which end up in $\mathcal{A}$. Clearly, the resulting partition is close to the one by the isocommittor function $\frac{1}{2}$ shown in Fig. 22, which indicates that the temperature is small enough so that it does not really affect this partition, except for wiping out the most external strips in the left and right corners in Fig. 23 (though this wiping effect is also due to the external boundary conditions imposed when solving for $q(x,v)$ and is less pronounced in the low friction case, see Fig. 26). Of
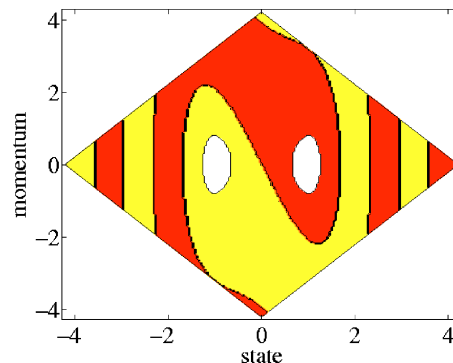

FIG. 23. Partition into regions that are asymptotically attracted to sets A or B, respectively, for the noise-free Langevin equation (30). Notice the similarity in the core with the partition by the isocommittor $\frac{1}{2}$ surface shown in the lower picture in Fig. 22.

course, in the absence of noise, there is no reaction, so the noise-free Langevin equation (30) is limited in the information that it can provide about the reaction and the full arsenal of TPT remains necessary to understand it.

The probability density function of reactive trajectories $\varrho_{\mathcal{AB}}(x,v)$ is shown in Fig. 24. As expected we observe that the distribution is peaked around a point with $x=0$ and $v>0$, that is, around the maximum of the potential but in the region of positive velocities since these are needed to go from $\mathcal{A}$ to $\mathcal{B}$. The reaction tube from $\mathcal{A}$ to $\mathcal{B}$ is shown in Fig. 25. This tube too indicates that the reaction pathway is asymmetric in the velocity (and, in particular, the reaction from $\mathcal{A}$ to $\mathcal{B}$ studied here is different from the one from $\mathcal{B}$ to $\mathcal{A}$—the reaction tube for the latter can be visualized by flipping Fig. 25 upside down, that is, by reverting the velocity)
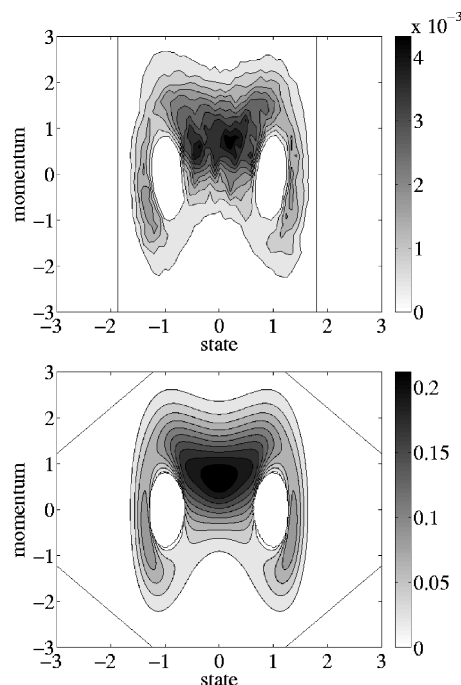

FIG. 24. Contour plot of the probability density function of reactive trajectories $\varrho_{\mathcal{AB}}(x,v)$ when $\beta=1$, $\gamma=1$. Upper: Result via DNS based on 300 reactive trajectories and a 40×40 box decomposition of the domain. Lower: Results from TPT.
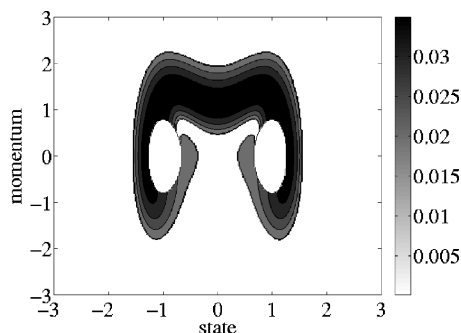
FIG. 25. Reaction tube based on streamlines of the probability current colored according to the intensity of the probability current on the dividing surface $S=\{(0,v):-3 \leq v \leq 3\}$. Results for $\beta=1$, $\gamma=1$.

C. Low friction case, $\gamma=0.001$

When the friction is as low as $\gamma=0.001$, Langevin dynamics is now close to Hamiltonian dynamics. Nevertheless, at sufficiently long time scales the damping will force the dynamics to get attracted to the vicinity of the minima of the energy landscape which lie inside the states $\mathcal{A}$ and $\mathcal{B}$, and the noise will eventually induce reactions between these states. Figure 26 shows the committor function $q(x,v)$ and the decomposition of the domain into the two regions $\{(x,v):q(x,v)<0.5\}$ and $\{(x,v):q(x,v)>0.5\}$ (dark gray) in the low friction case. Figure 27 shows the probability density function of reactive trajectories $\varrho_{AB}(x,v)$ and the reaction tube. In the present case, the streamlines of the probability current of the reactive trajectories (not shown) are very winding around the states $\mathcal{A}$ and $\mathcal{B}$ and turn out to be difficult to compute accurately.
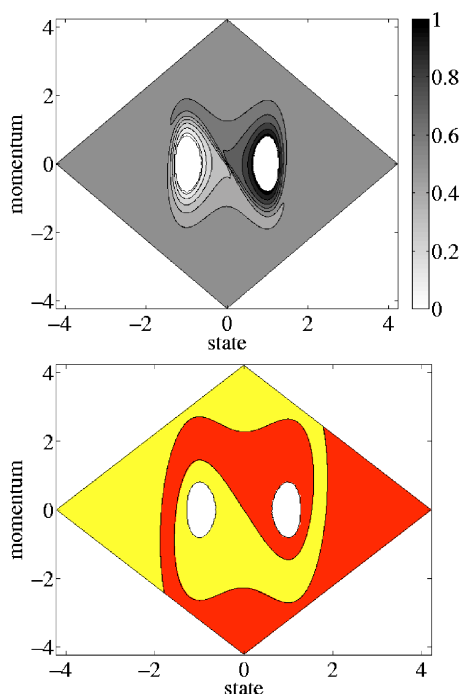

FIG. 26. Upper: Contour plot of the committor function $q(x,v)$ in the low friction case. Lower: Decomposition of the domain into the two regions $\{(x,v):q(x,v)<0.5\}$ (light gray) and $\{(x,v):q(x,v)>0.5\}$ (dark gray). The dividing curve is the isocommittor $\frac{1}{2}$ surface. Results for $\beta=1$, $\gamma=0.001$.
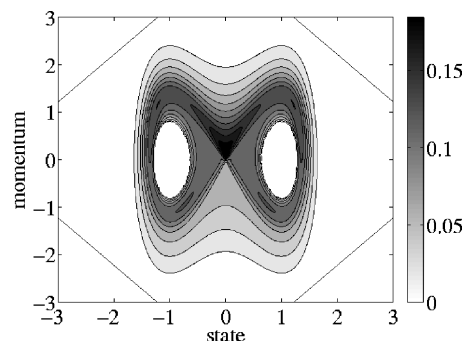

FIG. 27. Contour plot of the probability density function of reactive trajectories $\rho_{AB}(x,v)$. Result for $\beta=1$, $\gamma=0.001$.

VIII. OUTLOOK

In this paper, we have presented transition path theory (TPT) and illustrated this theory on some simple low dimensional examples. It was shown that knowing the committor function, the probability density function of the reactive trajectories, their probability current, and the streamlines of this current allows one to arrive at a complete understanding of the mechanism of the reaction. It also permits to compute its rate. As mentioned earlier, the examples chosen here, while already fairly rich, are very simplistic compared to those encountered in real applications. In particular, in realistic situations where the dimensionality of the problem is large it becomes prohibitively expensive to solve the backward Kolmogorov equations (12) and (21) by the numerical techniques based on finite differences that we used here. Nevertheless, we firmly believe that TPT is the right theoretical framework to understand the mechanism of the reaction even in much more complicated systems. In such systems, alternative numerical techniques will have to be developed to solve (12) and (21), based, e.g., on identifying a key set of collective variables sufficient to parametrize the committor function and, thereby, the mechanism of the reaction. The string method is one such technique that has already proven successful on realistic examples from material sciences[16,17] and molecular biology,[19,20] but, clearly, the scope of TPT goes beyond the string method and we certainly hope that the theory will serve as a guide to develop other numerical techniques to understand rare events in complicated systems.

APPENDIX: MORE ON TRANSITION PATH THEORY

Here we give some additional material about TPT; for more details, see Refs. 13 and 14.

Consider a system whose dynamics is governed by the following stochastic differential equation:

$$\dot{z}_i(t) = b_i(z(t)) + \sqrt{2} \sum_{j=1}^{m} \sigma_{ij} \eta_j(t), \quad i = 1, \dots, m, \qquad \text{(A1)}$$

where $b(x) = (b_1(z), \dots, b_m(z))^T \in \mathbb{R}^m$ is the drift vector,

$$\sigma = \begin{pmatrix} \sigma_{11} & \cdots & \sigma_{1m} \\ \vdots & \ddots & \vdots \\ \sigma_{m1} & \cdots & \sigma_{mm} \end{pmatrix} \in \mathbb{R}^m \times \mathbb{R}^m \qquad \text{(A2)}$$

is the square root of the diffusion tensor, and $\eta(t) = (\eta_1(t), \dots, \eta_m(t))^T \in \mathbb{R}^m$ is an m-dimensional white noise, i.e., a Gaussian process with mean 0 and covariance $\langle \eta_i(t) \eta_j(s) \rangle = \delta_{ij} \delta(t-s)$. Clearly, both (1) and (13) can be put into the form of (A1) with appropriate identification.

Denoting by $\rho(z)$ the equilibrium probability density function of $z(t)$, i.e., the probability density to find a trajectory (reactive or not) at position z at time t, $\rho(z)$ is the steady solution of the forward Kolmogorov equation (also known as Fokker-Planck equation),

$$0 = -\sum_{i=1}^{m} \frac{\partial}{\partial z_i} (b_i(z)\rho(z)) + \sum_{i,j=1}^{m} \frac{\partial^2}{\partial z_i \partial z_j} (a_{ij}(z)\rho(z)), \qquad \text{(A3)}$$

where $a(z) = a^T(z) = \sigma(z)\sigma^T(z) \in \mathbb{R}^m \times \mathbb{R}^m$ is the non-negative-definite diffusion tensor. In addition, if $A \subset \mathbb{R}^m$ and $B \subset \mathbb{R}^n$ denote the reactant and product states, respectively, the forward committor function $q(z)$ giving the probability that the trajectory starting from $z \in \mathbb{R}^n \setminus (A \cup B)$ reaches first B rather than A satisfies the backward Kolmogorov equation associated with (A1),

$$0 = \sum_{i=1}^{m} b_i(z) \frac{\partial q(z)}{\partial z_i} + \sum_{i,j=1}^{m} a_{ij}(z) \frac{\partial^2 q(z)}{\partial z_i \partial z_j},$$

$$q(z)|_{z \in \partial A} = 0, \qquad q(z)|_{z \in \partial B} = 1. \qquad \text{(A4)}$$

Similarly, the backward committor function $q_b(z)$ giving the probability that the trajectory arriving at z at time t came last from A rather than B satisfies the backward Kolmogorov equation associated with the time reversed trajectory,

$$0 = \sum_{i=1}^{m} b_i^R(z) \frac{\partial q_b(z)}{\partial z_i} + \sum_{i,j=1}^{m} a_{ij}(z) \frac{\partial^2 q_b(z)}{\partial z_i \partial z_j},$$

$$q_b(z)|_{z \in \partial A} = 1, \qquad q_b(z)|_{z \in \partial B} = 0, \qquad \text{(A5)}$$

where

$$b_i^R(z) = -b_i(z) + \frac{2}{\rho(z)} \sum_{j=1}^{m} \frac{\partial}{\partial z_i} (a_{ij}(z)\rho(z)). \qquad \text{(A6)}$$

Letting $z(t) - \infty < t < \infty$ be a long ergodic trajectory solution of (A1), the ensemble of reactive trajectories is defined as

ensemble of reactive trajectories

$$= \{z(t) : t \in \mathcal{R}\}, \quad \text{where } t \in \mathcal{R} \quad \text{if and only if}$$

$$z(t) \notin A \cup B, \quad z(t_{AB}^+(t)) \in B, \quad \text{and } z(t_{AB}^-(t)) \in A, \qquad \text{(A7)}$$

where

$$t_{AB}^+(t) = \text{smallest } t' \geqslant t \text{ such that } z(t') \in A \cup B,$$
$$t_{AB}^-(t) = \text{largest } t' \leqslant t \text{ such that } z(t') \in A \cup B. \qquad \text{(A8)}$$

Each continuous piece of trajectory going from A to B in the ensemble (A7) is a specific reactive trajectory. The main objects of TPT are then defined of terms of the reactive trajectories and expressed in terms of $\rho(z)$, $q(z)$, and $q_b(z)$ as follows.

The probability density function of reactive trajectories $\rho_{AB}(z)$ is defined such that, giving any observable $\phi(z)$, we have

$$\lim_{T \to \infty} \frac{\int_{\mathcal{R} \cap [-T,T]} \phi(z(t)) dt}{\int_{\mathcal{R} \cap [-T,T]} dt} = \int_{\Omega_{AB}} \phi(z) \rho_{AB}(z) dz, \qquad \text{(A9)}$$

where $\Omega_{AB} = \mathbb{R}^m \setminus (A \cup B)$. From the argument given in Sec. II, it can be expressed in terms of $\rho(z)$, $q(z)$, and $q_b(z)$ as

$$\rho_{AB}(z) = Z_{AB}^{-1} q(z) q_b(z) \rho(z), \qquad \text{(A10)}$$

where Z_{AB} is the probability that the trajectory be reactive at time t,

$$Z_{AB} = \int_{\Omega_{AB}} q(z) q_b(z) \rho(z) dz. \qquad \text{(A11)}$$

(A10) reduces to (5) when the dynamics is overdamped and to (15) when it is Langevin.

The probability current of reactive trajectories $J_{AB}(z)$ is the vector field defined in Ω_{AB} which is such that, given any surface $S \subset \Omega_{AB}$ which is the boundary of a region Ω_S, the surface integral of $J_{AB}(z)$ over S gives the probability flux of reactive trajectories across S. More precisely,

$$\lim_{s \to 0^+} \frac{1}{s} \lim_{T \to \infty} \frac{1}{2T} \int_{\mathcal{R} \cap [-T,T]} (\chi_{\Omega_S}(z(t)) \chi_{\mathbb{R}^m \setminus \Omega_S}(z(t+s))$$
$$- \chi_{\mathbb{R}^m \setminus \Omega_S}(z(t)) \chi_{\Omega_S}(z(t+s))) dt$$
$$= \int_S \hat{n}_S(z) J_{AB}(z) d\sigma_S(z), \qquad \text{(A12)}$$

where, giving any set $C \subset \mathbb{R}^m$, $\chi_C(z) = 1$ if $z \in C$ and $\chi_C(z) = 0$ otherwise, and $\hat{n}_S(z)$ is the unit normal on S pointing outward Ω_S and $d\sigma_S(z)$ is the surface element on S. As shown next, $J_{AB}(z)$ can be expressed componentwise as

$$J_{AB,i}(z) = q(z) q_b(z) J_i(z) + q_b(z) \rho(z) \sum_{j=1}^{m} a_{ij}(z) \frac{\partial q(z)}{\partial z_j}$$
$$- q(z) \rho(z) \sum_{j=1}^{m} a_{ij}(z) \frac{\partial q_b(z)}{\partial z_j}, \qquad \text{(A13)}$$

where $J(z) = (J_1(z), \dots, J_m(z))^T$ is the equilibrium probability current,

$$J_i(z) = b_i(z) \rho(z) - \sum_{j=1}^{m} \frac{\partial}{\partial z_j} (a_{ij}(z)\rho(z)). \qquad \text{(A14)}$$

(A13) reduces to (6) when the dynamics is overdamped and to (17) when it is Langevin. To derive (A13), we take first the limit as $T \to \infty$ in (A12) using ergodicity to obtain

$$\lim_{s \to 0^+} \frac{1}{s} \left(\int_{\Omega_S} \rho(z) q_b(z) \mathbf{E}_z(q(z(s)) \chi_{\mathbb{R}^m \setminus \Omega_S}(z(s)))) \right) dz$$

$$- \int_{\mathbb{R}^m \setminus \Omega_S} \rho(z) q_b(z) \mathbf{E}_z(q(z(s)) \chi_{\Omega_S}(z(s))) dz,$$

$$= \int_S \hat{n}_S(z) J_{AB}(z) d\sigma_S(z), \tag{A15}$$

where $\mathbf{E}_z$ denotes expectation conditional on $z(0) = z$. Taking the limit as $s \to 0^+$ can now be done using

$$\lim_{t \to 0^+} \frac{1}{t}(\mathbf{E}_z \phi(z(t)) - \phi(z)) = \sum_{i=1}^m b_i(z) \frac{\partial \phi(z)}{\partial z_i}$$

$$+ \sum_{i,j=1}^m a_{ij}(z) \frac{\partial^2 \phi(z)}{\partial z_i \partial z_j}$$

$$\equiv (L\phi)(z),$$

where $\phi(z)$ is any suitable observable. However, taking the limit on (A15) is somewhat tricky because of the presence of the discontinuous functions $\chi_{\Omega_S}(z)$ and $\chi_{\mathbb{R}^m \setminus \Omega_S}(z)$. The proper way to avoid ambiguities on how to interpret the derivatives of $\chi_{\Omega_S}(z)$ and $\chi_{\mathbb{R}^m \setminus \Omega_S}(z)$ is to mollify these functions, that is, replace them by functions varying rapidly on S but smooth, then let $s \to 0^+$ and finally remove the mollification. Let then $f_\delta(z)$ be a smooth function which is 1 in Ω_S at a distance δ from S, 0 out of Ω_S at a distance δ from S, and varies rapidly but smoothly from 0 to 1 in the strip of size 2δ around S. Thus (A15) is the limit as $\delta \to 0$ of

$$I_\delta = \lim_{s \to 0^+} \frac{1}{s} \int_{\mathbb{R}^m} \rho(z) q_b(z) (f_\delta(z) \mathbf{E}_z(q(z(s))(1 - f_\delta(z(s))))$$

$$- (1 - f_\delta(z)) \mathbf{E}_z(q(z(s)) f_\delta(z(s)))) dz.$$

Inserting

$$0 = - \rho(z) q_b(z) f_\delta(z) (q(z)(1 - f_\delta(z)))$$

$$+ \rho(z) q_b(z) (1 - f_\delta(z)) (q(z) f_\delta(z)),$$

under the integral then letting $s \to 0^+$, we obtain

$$I_\delta = \int_{\mathbb{R}^m} \rho(z) q_b(z) (f_\delta(z) (L(q(1 - f_\delta)))(z)$$

$$- (1 - f_\delta(z)) (L(q f_\delta))(z)) dz.$$

Expanding the integrand, several terms cancel and we are simply left with

$$I_\delta = - \int_{\mathbb{R}^m} \rho(z) q_b(z) (L(q f_\delta))(z) dz.$$

Using the explicit form for L and expanding, this is

$$I_\delta = - \int_{\mathbb{R}^m} \rho(z) q_b(z) \left(f_\delta(z) Lq(z) \right.$$

$$+ \sum_{i,j=1}^m a_{ij}(z) \frac{\partial}{\partial z_i} \left(q(z) \frac{\partial f_\delta(z)}{\partial z_j} \right)$$

$$+ \left. \sum_{i=1}^m \frac{\partial f_\delta(z)}{\partial z_i} \left(b_i(z) q(z) + \sum_{j=1}^m a_{ij}(z) \frac{\partial q(z)}{\partial z_j} \right) \right) dz.$$

By (A4), $Lq(z) = 0$ and integrating by parts the second term in the parentheses under the integral, we arrive at

$$I_\delta = - \int_{\mathbb{R}^m} \sum_{i=1}^m \frac{\partial f_\delta(z)}{\partial z_i} \left(q(z) q_b(z) J_i(z) \right.$$

$$+ q_b(z) \rho(z) \sum_{j=1}^m a_{ij}(z) \frac{\partial q(z)}{\partial z_j}$$

$$- \left. q(z) \rho(z) \sum_{j=1}^m a_{ij}(z) \frac{\partial q_b(z)}{\partial z_j} \right) dz.$$

Now let $\delta \to 0$ and recall that for any suitable $F(z) = (F_i(z), \dots, F_n(z))^T$,

$$\lim_{\delta \to 0} \int_{\mathbb{R}^m} \sum_{i=1}^m \frac{\partial f_\delta(z)}{\partial z_i} F_i(z) dz = - \lim_{\delta \to 0} \int_{\mathbb{R}^m} f_\delta(z) \sum_{i=1}^n \frac{\partial F_i(z)}{\partial z_i} dz$$

$$= - \int_{\Omega_S} \sum_{i=1}^m \frac{\partial F_i(z)}{\partial z_i} dz$$

$$= - \int_S \sum_{i=1}^n \hat{n}_{S,i}(z) F_i(z) d\sigma_S(z),$$

where the first equality follows by integration by parts, the second by definition of $f_\delta(z)$, and the third by the divergence theorem. Using this result, we conclude that the limit of the expression above for I_δ as $\delta \to 0$ is the surface integral of the current $J_{AB}(z)$ given in (A13), as claimed.

The current $J_{AB}(z)$ is divergence-free, and its integral over any dividing surface $S \subset \Omega_{AB}$ gives the reaction rate,

$$k_{AB} = \int_S \hat{n}_S(z) J_{AB}(z) d\sigma_S(z) \quad (\text{dividing } S), \tag{A16}$$

where $\hat{n}_S(z)$ is the unit normal to S pointing toward B. Letting N_T^R be the number of reactive trajectories observed during the time interval $[-T, T]$ in the ensemble (A7), k_{AB} is the limit,

$$k_{AB} = \lim_{T \to \infty} \frac{N_T^R}{2T}, \tag{A17}$$

i.e., it gives the exact mean frequency at which the reactive trajectories are observed within a given trajectory.

The expression (A17) for the rate can be simplified and transformed into a volume integral over Ω_{AB},

$$k_{AB} = \int_{\Omega_{AB}} \rho(z) \sum_{i,j=1}^{m} a_{ij}(z) \frac{\partial q(z)}{\partial z_i} \frac{\partial q(z)}{\partial z_j} dz, \qquad (A18)$$

which reduces to (9) when the dynamics is overdamped and to (19) when it is Langevin. To check that (A18) gives the rate, let $S(\zeta) = \{z : q(z) = \zeta\}$ be the (forward) isocommittor surface with committor value $\zeta \in [0,1]$, and consider the integral

$$A(\zeta) = \int_{S(\zeta)} \rho(z) \sum_{i,j=1}^{m} \hat{n}_{S(\zeta),i}(z) a_{ij}(z) \frac{\partial q(z)}{\partial z_j} d\sigma_{S(\zeta)}(z).$$

Since $S(0) \equiv \partial A$ is easy to see from (A17) and (A16) with $S = \partial A$ that

$$A(0) = \int_{\partial A} \rho(z) \sum_{i,j=1}^{m} \hat{n}_{\partial A,i}(z) a_{ij}(z) \frac{\partial q(z)}{\partial z_j} d\sigma_{\partial A}(z) \equiv k_{AB},$$

where we used $q(z) = 0$ and $q_b(z) = 1$ on ∂A. Next, we show that $A(\zeta) = A(0) = k_{AB}$ for all $\zeta \in [0,1]$. Using the Dirac delta function we can express $A(\zeta)$ as

$$A(\zeta) = \int_{\mathbb{R}^m} \rho(z) \sum_{i,j=1}^{m} \frac{\partial q(z)}{\partial z_i} a_{ij}(z) \frac{\partial q(z)}{\partial z_j} \delta(q(z) - \zeta) dz,$$

and hence

$$\frac{dA(\zeta)}{d\zeta} = -\int_{\mathbb{R}^m} \rho(z) \sum_{i,j=1}^{m} \frac{\partial q(z)}{\partial z_i} a_{ij}(z) \frac{\partial q(z)}{\partial z_j} \delta'(q(z) - \zeta) dz$$

$$= -\int_{\mathbb{R}^m} \rho(z) \sum_{i,j=1}^{m} \frac{\partial q(z)}{\partial z_i} a_{ij}(z) \frac{\partial}{\partial z_j} \delta(q(z) - \zeta) dz.$$

Integrating by parts, this gives

$$\frac{dA(\zeta)}{d\zeta} = \int_{\mathbb{R}^m} \rho(z) \sum_{i,j=1}^{m} a_{ij}(z) \frac{\partial^2 q(z)}{\partial z_i \partial z_j} \delta(q(z) - \zeta) dz + \int_{\mathbb{R}^m} \sum_{i,j=1}^{m} \frac{\partial q(z)}{\partial z_i} \frac{\partial}{\partial z_j} (a_{ij}(z) \rho(z)) \delta(q(z) - \zeta) dz$$

$$= -\int_{\mathbb{R}^m} \rho(z) \sum_{i=1}^{m} b_i(z) \frac{\partial q(z)}{\partial z_i} \delta(q(z) - \zeta) dz + \int_{\mathbb{R}^m} \sum_{i,j=1}^{m} \frac{\partial q(z)}{\partial z_i} \frac{\partial}{\partial z_j} (a_{ij}(z) \rho(z)) \delta(q(z) - \zeta) dz,$$

where in the second step we used (A4). Using the definition (A14) for the equilibrium current $J(z)$, the two integrals in the last equality can be recombined into

$$\frac{dA(\zeta)}{d\zeta} = -\int_{\mathbb{R}^m} \sum_{i=1}^{m} \frac{\partial q(z)}{\partial z_i} J_i(z) \delta(q(z) - \zeta) dz$$

$$= -\int_{S(\zeta)} \sum_{i=1}^{m} n_{S(\zeta),i}(z) J_i(z) d\sigma_{S(\zeta)}(z) = 0, \qquad (A19)$$

where in the last equality we use the fact that the probability flux of the regular (by opposition to reactive) trajectories through any surface is zero at equilibrium. (A19) implies that $A(\zeta) = A(0) = k_{AB}$ for all $\zeta \in [0,1]$, as claimed. Hence, $\int_0^1 A(\zeta) d\zeta = k_{AB}$ which gives

$$\int_0^1 \int_{\mathbb{R}^m} \rho(z) \sum_{i,j=1}^{m} \frac{\partial q(z)}{\partial z_j} a_{ij}(z) \frac{\partial q(z)}{\partial z_j} \delta(q(z) - \zeta) dz d\zeta$$

$$= \int_{\Omega_{AB}} \rho(z) \sum_{i,j=1}^{m} \frac{\partial q(z)}{\partial z_j} a_{ij}(z) \frac{\partial q(z)}{\partial z_j} dz = k_{AB}.$$

This is (A18).

[1] H. Eyring, J. Chem. Phys. **3**, 107 (1935).
[2] E. Wigner, Trans. Faraday Soc. **34**, 29 (1938).
[3] T. Yamamoto, J. Chem. Phys. **33**, 281 (1960).
[4] C. H. Bennett, in *Algorithms for Chemical Computation*, eds. A. S. Nowick and J. J. Burton (ACS Symposium Series No. 46, **63**, 1977).
[5] D. Chandler, J. Appl. Phys. **68**, 2959 (1978).
[6] E. Vanden-Eijnden and F. Tal, J. Chem. Phys. **123**, 184103 (2005).
[7] F. Tal and E. Vanden-Eijnden, Nonlinearity **19**, 501 (2006).
[8] P. G. Bolhuis, D. Chandler, C. Dellago, and P. Geissler, Annu. Rev. Phys. Chem. **59**, 291 (2002).
[9] C. Dellago, P. G. Bolhuis, and P. L. Geissler, Adv. Chem. Phys. **123**, 1 (2002).
[10] R. Elber, A. Ghosh, and A. Cárdenas, Acc. Chem. Res. **35**, 396 (2002).
[11] R. Elber, A. Ghosh, A. Cárdenas, and H. Stern, Adv. Chem. Phys. **126**, 93 (2003).
[12] G. Hummer, J. Chem. Phys. **120**, 516 (2004).
[13] W. E and E. Vanden-Eijnden, J. Stat. Phys. (in press).
[14] E. Vanden-Eijnden, in *Computer Simulations in Condensed Matter: from Materials to Chemical Biology*, edited by M. Ferrario, G. Ciccotti, and K. Binder (Springer-Verlag, Berlin, in press).
[15] W. E, W. Ren, and E. Vanden-Eijnden, Phys. Rev. B **66**, 052301 (2002).
[16] W. E, W. Ren, and E. Vanden-Eijnden, J. Appl. Phys. **93**, 2275 (2003).
[17] W. E, W. Ren, and E. Vanden-Eijnden, J. Phys. Chem. B **109**, 6688 (2005).
[18] W. E, W. Ren, E. Vanden-Eijnden, Chem. Phys. Lett. **413**, 242 (2005).
[19] W. Ren, E. Vanden-Eijnden, P. Maragakis, and W. E, J. Chem. Phys. **123**, 134109 (2005).
[20] L. Maragliano, A. Fischer, E. Vanden-Eijnden, and G. Ciccotti, J. Chem. Phys. (to be published).
[21] S. Park, M. Sener, D. Lu, and K. Schulten, J. Chem. Phys. **119**, 1313 (2003).
[22] R. Durrett, *Stochastic Calculus* (CRC, Boca Raton, FL, 1996).
[23] P. Metzner, C. Schütte, E. Vanden-Eijnden, and R. Kornhuber (unpublished).
[24] E. Vanden-Eijnden and G. Ciccotti, Chem. Phys. Lett. (submitted).
[25] M. I. Freidlin and A. D. Wentzell, *Random Perturbations of Dynamical Systems* (Springer-Verlag, New York, 1984).
[26] C. Schütte, J. Walter, C. Hartmann, and W. Huisinga, Multiscale Model. Simul. **2**, 501 (2004).
[27] P. Deuflhard and C. Schütte, Proc. Appl. Math. Mech. **116**, 91 2004).